Published in final edited form as:
Glia. 2010 April 15; 58(6): 665–678. doi:10.1002/glia.20953.

Olfactory ensheathing cell membrane properties are shaped by connectivity

Lorena Rela[1], **Angelique Bordey**[1,3], and **Charles A. Greer**[1,2]

[1]Department of Neurosurgery, Yale University School of Medicine, PO Box 208082, New Haven, CT 06520

[2] Department of Neurobiology, PO Box 208082, New Haven, CT 06520

[3]Cellular and Molecular Physiology, PO Box 208082, New Haven, CT 06520

Abstract

Olfactory ensheathing cells (OECs) have been repeatedly implicated in mediating plasticity, particularly *in situ* in the olfactory nerve where they support the extension of olfactory sensory neuron (OSNs) axons from the olfactory epithelium to the olfactory bulb (OB). OECs are specialized glia whose processes surround OSN axon fascicles within the olfactory nerve and across the OB surface. Despite their purported importance in promoting axon extension, and following transplants, little is known about either morphology or biophysical properties of OECs *in situ*. In particular, cell-cell interactions that may influence OEC function are largely unexplored. Here, we studied OEC connectivity and morphology in slice preparations, preserving tissue structure and cell-cell interactions. Our analyses showed that OECs form a matrix of cellular projections surrounding axons, unique among glia, and express high levels of connexin-43. Lucifer Yellow injections revealed selective dye coupling among small subgroups of OECs. Two types of OECs were biophysically distinguished with whole cell voltage clamp recordings: 1) with low input resistance (Ri), linear current profiles, and frequently dye coupled; and 2) with high Ri, non-linear current profiles, and infrequent dye coupling. Pharmacological blockade of gap junctions changed OEC membrane properties such that linear OECs became non-linear. Double recordings indicated that the appearance of the non-linear current profile was associated with the loss of electrical coupling between OECs. We conclude that the diversity of OEC current profiles can be explained by differences in gap junction connectivity and discuss implications of this diversity for OEC influences on axon growth and excitability.

Keywords

Olfactory bulb; Gap junctions; Connexins; Dye coupling; Electrical coupling

Introduction

Profound neurogenesis occurs in restricted areas of the adult mammalian brain under physiological conditions (Zhao et al. 2008). In the olfactory system, central neurogenesis provides subventricular zone-derived interneurons to the OB (Altman 1969; Carleton et al. 2003; Whitman and Greer 2007a; Whitman and Greer 2007b). Peripheral neurogenesis in the olfactory epithelium produces OSNs throughout life (Caggiano et al. 1994; Graziadei and Graziadei 1979). OSN axons form the olfactory nerve, coalesce into fascicles from

Corresponding author: Charles A. Greer, Ph.D., Department of Neurosurgery, Yale University School of Medicine, P.O. Box 208082, New Haven, CT 06520-8082, Telephone – 203.785.4034, charles.greer@yale.edu.

OSNs expressing the same odor receptor, and converge into topographically defined glomeruli, in the OB (Mombaerts et al. 1996; Ressler et al. 1994; Treloar et al. 2002; Vassar et al. 1994). The olfactory nerve is unique since new OSN axons re-innervate the central nervous system (CNS) after ablation (Gogos et al. 2000; Harding and Wright 1979).

While the mechanisms underlying sustained axon growth in the olfactory nerve remain elusive, one difference between CNS regions that are permissive or non-permissive for axonal growth may lie in the molecular phenotype of glial cells and the composition of the extracellular matrix (Cafferty et al. 2007; Liesi 1985). OECs are non-myelinating glial cells that wrap and interdigitate between OSN axon fascicles (Doucette 1993), and share properties of astrocytes and Schwann cells, differing from both (Doucette 1990; Vincent et al. 2005). OECs promote axon extension when co-cultured with neurons (Kafitz and Greer 1999; Runyan and Phelps 2009) and, in animal models of spinal cord or nerve injury, OEC transplants can improve axonal regeneration (Barnett and Riddell 2007; Bartolomei and Greer 2000; Raisman and Li 2007; Schwab 2002).

Glia-glia communication is important for the function of neighboring neurons. In hippocampal astrocytes, gap junction communication is essential for the trafficking of metabolites that sustain synaptic function (Rouach et al. 2008). The phenotype and effects of OECs on axon growth have been studied primarily in culture or transplants (Li et al. 1998; Raisman and Li 2007). Given the evidence suggesting that OECs promote axon plasticity and outgrowth, it is essential that their role *in situ*, where phenotype and cell-cell interactions remain unaltered, be more fully explored, both regarding general properties of axon extension as well as the complex sorting and coalescence exhibited by the ~1,000 subpopulations of OSN axons.

To better understand cell-cell interactions with potential importance for OEC function, we examined morphological, ultrastructural and physiological OEC properties using methods that preserved the OEC phenotype and cellular interactions found *in vivo*. We show that OECs are morphologically complex and unique and show for the first time that OECs form functional gap junctions *in situ*, presumably mediated by connexin-43 (Cx43). Gap junction coupling allows OECs to form domains, dramatically altering their biophysical properties. We show compelling evidence that the diversity of OEC current vs. voltage profiles can be explained by differences in gap junction connectivity and discuss the implications for the functions of associated OSN axons.

Materials and methods

Animals and tissue processing

To prepare acute slices for electrophysiological recording, CD-1 mice [postnatal day 14 (P14) to P21] (Charles River, Wilmington, MA) were anesthetized with sodium pentobarbital (80 mg/kg, i.p.; Nembutal; Abbott Laboratories, North Chicago, IL) prior to dissection. For immunohistochemistry on thick tissue sections, we used CD-1 mice and S100-GFP K mice (P14 to P28), expressing GFP under the regulatory elements of S100B, provided by Dr Wesley Thompson, University of Texas at Austin (Zuo et al. 2004). The animals were anesthetized and intracardially perfused with 4% paraformaldehyde (PFA) in phosphate-buffered saline (PBS), pH 7.4. The brains were dissected, fixed for 2 hours at 4°C, rinsed in PBS, embedded in 1.5% agarose in distilled water and horizontally cut using a vibratome (250 μm sections) in cold phosphate buffer (pH 7.4). For electron microscopy, CD-1 mice (P17) were anesthetized and intracardially perfused with 2% glutaraldehyde and 4% PFA in PBS, and processed for electron microscopy. All procedures were approved by the Yale University's Animal Care and Use Committee and conform to NIH guidelines.

Acute slice preparation

Brain slices containing the OB were prepared as previously reported (Wang et al. 2003a; Wang et al. 2003b). Anesthetized mice were decapitated, the brain quickly removed and chilled (0–4 °C) in 95% O_2-5% CO_2-saturated sucrose-based artificial cerebrospinal fluid (ACSF) containing (in mM): 220 Sucrose, 2.5 KCl, 1 $CaCl_2$, 6 $MgCl_2$, 1.25 NaH_2PO_4, 26 $NaHCO_3$ and 10 glucose. The brain was ventrally glued (horizontal slices) or embedded in 4% low-melting point agarose in ACSF and glued (sagittal slices) to a vibratome stage and 250 μm slices were cut. The slices recovered at room temperature for >1 hour in ACSF containing (in mM): 125 NaCl, 2.5 KCl, 2 $CaCl_2$, 1.1 $MgCl_2$, 1.25 NaH_2PO_4, 26 $NaHCO_3$ and 10 glucose, pH 7.4. After recovery, slices were placed in a flow-through chamber, held in position by a harp (Warner Instruments, Hamden, CT), and continuously superfused with oxygenated ACSF at room temperature. Patch-clamp experiments were performed on an upright Olympus BX51WI microscope (Optical Analysis, Nashua, NH) with Nomarski phase-contrast, water-immersion and fluorescence optics (60x; numerical aperture, 0.9), and infra-red illumination.

Electrophysiological recordings and drug applications

Cells were visually identified in the olfactory nerve layer of the OB. Although interfascicular astrocytes are reported in the olfactory nerve and nerve layer (Doucette, 1984), OECs constitute greater than 95% of glial cells in this layer (Valverde and Lopez-Mascaraque 1991; our unpublished observations). Whole cell patch-clamp recordings were obtained as previously described (Bordey and Sontheimer 2000). Patch pipettes were pulled from thin-walled borosilicate glass (1.50 / 1.10 mm outside / inside diameters, respectively; BF150-110-10; Sutter Instrument, Novato, CA) on a P-97 puller (Sutter). Pipette resistance was 5-10 MΩ when filled with intracellular solution (in mM): 130 KCl, 0.25 $CaCl_2$, 4 $MgCl_2$, 5 EGTA, 10 HEPES, 4 K_2ATP and 0.5 Na_2GTP, pH 7.3, adjusted with KOH. Osmolarity of the intracellular and extracellular solutions were 295-300 and 305-310 mOsm, respectively, measured with a vapor pressure osmometer 5520 (Wescor, Logan, UT). To label cells, 0.1% Lucifer Yellow (LY, dilithium salt, Invitrogen/Molecular Probes) was added to the pipette solution. Recordings were performed using a MultiClamp 700B amplifier (Molecular Devices, Sunnyvale, CA). Current signals were low-pass filtered (4 kHz) and digitized online (10 kHz) using a Digidata 1440A board (Molecular Devices) interfaced with an IBM-compatible computer. Data acquisition, storage, and analysis were done using PClamp version 10 (Molecular Devices). Capacitance and series resistance compensation (at least 60%) were used to minimize voltage errors. Settings were determined by compensating the transients of a small (10-mV) 50 ms hyperpolarizing voltage step. The capacitance reading of the amplifier was used for the whole cell capacitance. Leak conductance was not subtracted. Resting potential (Vr) was measured in zero-current mode. Meclofenamic acid (MFA, Sigma Chemical Co. St. Louis, MO) diluted in ACSF was applied by a rapid bath application system. For double recordings, a cell was patched and LY was let to diffuse. A dye-coupled cell was chosen as the second cell to increase the probability of observing electrical coupling.

Visualization of LY-filled cells and Immunohistochemistry

DIC and fluorescence images were acquired with a video capture device (ATSC-TV 310U, Kworld, CA). Slices with LY-filled cells were fixed overnight in 4% PFA in PBS at 4°C, washed 3 times for 10 minutes with PBS, incubated for 30 minutes with the nuclear marker DRAQ5 (1:1000, Alexis Biochemicals, San Diego, CA), washed in PBS for 10 minutes and mounted with Gel-Mount (BioMeda, Foster City, CA) on glass coverslips. Tissue sections were immunostained free-floating with gentle shaking. The tissue was blocked for 2 hours in blocking buffer (2% bovine serum albumin and 0.3% Triton X-100, American Bioanalytical, Natick, MA, in PBS). Primary antibodies [rabbit anti-BLBP, AB9558; rat anti-NCAM,

MAB310; mouse anti-connexin 32 (Cx32), MAB3069; and rabbit anti-Cx26, AB1717 from Chemicon/Millipore; rabbit anti-Cx43 71-0700 from Zymed/Invitrogen] diluted in blocking buffer were incubated overnight at room temperature. Sections were washed 3 times in 0.3% Triton X-100 in PBS for 10 minutes and incubated in secondary antibodies conjugated to Alexa Fluor (Invitrogen/Molecular Probes, Carlsbad, CA) and DRAQ5, diluted 1:1000 in blocking buffer for 2 hours at room temperature. Sections were washed as above, rinsed in PBS, mounted and coverslipped. Images were acquired with a Leica confocal microscope as z-stacks, with 0.2-1-μm steps between optical sections, using an oil-immersion objective (40×; numerical aperture, 1.25) and up to 4× digital zoom. Digital images were color balanced with Adobe Photoshop 8.0 (Adobe Systems, San Jose, CA). The composition of the images was not altered in any way.

Electron microscopy (EM)

Sections were processed as described previously (Montague and Greer 1999). Briefly, following dissection the OB was sectioned with a vibratome, post-fixed with osmium tetroxide, dehydrated through graded alcohols, and polymerized in Epon between glass slides and coverslips coated previously with Liquid Release Agent (Electron Microscopy Sciences, Fort Washington, PA). Smaller regions containing the olfactory nerve layer were removed and re-embedded on blank Epon blocks for thin sectioning and conventional electron microcopy. Thin sections (0.07-μm) were examined on a JEOL 1200 electron microscope (Peabody, MA) and photographed at primary magnifications of 6,000-15,000×. Gap junctions were photographed at 25,000-40,000× and were identified as apposed processes separated by about 2 nm appearing in cross section as a 7 layered structure (Brightman and Reese 1969).

Analysis of morphological data

Imaris 6.2.1 (Bitplane, Saint Paul, MN) was used for 3D-reconstructions of OECs. We did not include dye coupled cells in this analysis because diffusion of the dye to other cells resulted in a dimmer signal. We used a series of parameters to estimate OEC size and shape. First, we manually defined 3-dimensional points at the cell body and at the tips of OEC lamellae to determine segments, used as estimators of lamellar length. Second, we defined the longest distance between any pair of the former points as the cell main axis, used as reference to define a bounding box enclosing the cell with perpendicular planes. The dimensions of the box (length, width and depth) were used as indicators of cell shape. Finally, we rendered isosurfaces using local background subtraction (sphere diameter: 0.15-0.6-μm) and smoothing (grain size: 0.15-0.2-μm) to calculate the cell surface and volume. The threshold was adjusted manually.

For the analysis of dye-coupled clusters, we measured the 3-dimensional distance from the cell body of the injected cell to the cell bodies of each labeled cell with Imaris. To analyze the symmetry of OEC clusters, a segment was defined between the cell body of the recorded cell and the tip of the farthest reaching projection. The far-end of this segment was defined as the north pole of the cluster. A perpendicular plane to this segment at the opposite end (cell body of the recorded cell) was defined as the equator. The number of cells in the northern and southern hemispheres was counted manually with the aid of Imaris clipping planes, in a field containing the dye-filled cell at the center. To measure the dye intensity in the cells of a cluster, contour surfaces were defined with Imaris for each cell body and the average intensity was obtained inside each surface. Values were normalized to the average intensity in the injected cell.

For morphological analysis of OEC lacunae at the optical level, we manually outlined the spaces (lacunae) defined by fine projections of LY-filled OECs in single optical sections

using ImageJ (NIH). These regions of interest were fitted to ellipses, and the maximum and minimum diameters were averaged for each ellipse. For analysis of lacunae at the EM level we manually outlined OEC profiles (recognized by the electron dense appearance) with Corel Draw (Corel, Ottawa, Ontario, Canada), measured the maximum and minimum diameters of lacunae defined by OEC fine processes and averaged these two values.

To classify OECs as deep, intermediate or superficial we took a picture of each recorded slice at low magnification before pulling the recording pipette away, to mark the position of the recorded cell. We then divided the ONL in thirds (deep, intermediate and superficial) by drawing two lines parallel to the surface of the bulb. The inner limit of the ONL could be distinguished by a difference in contrast between the ONL and the glomerular layer. The tip of the pipette indicated in which of the three regions of the ONL each OEC was located.

Analysis of physiological data

Current amplitudes were measured either at the peak value or at the end of the voltage pulses applied to the recorded cells. When data were normalized, it was done relative to the maximum amplitude measured for each cell in control conditions. To assess the linearity of current vs. voltage (I/V) curves, we used the correlation coefficient (r^2) of a linear fit to the I/V curves in the range from -60 to 40 mV, the range in which outward voltage-dependent conductances activated. Ohm's Law was used to calculate input resistance (Ri) from the current elicited by a -10 mV voltage step (holding potential = -80 mV). The gap junction conductance, Gj, was calculated from double recordings as Gj = I/Vj, where I is the coupling current recorded in the non-stimulated cell in response to a voltage step to -120 mV in the stimulated cell (holding potential = -80 mV), and Vj is the difference in potential across the gap junction, estimated as the difference between the holding potential in the non-stimulated cell (-80 mV) minus the command voltage in the stimulated cell (-120 mV). This is likely an overestimation owing to spatial attenuation and remaining voltage errors associated with partial series resistance compensation.

Graphs and statistical analysis

Graphs and statistical analyses were done with Prism 4 (GraphPad, La Jolla, CA). Statistical values are informed in the text as mean ± standard error of the mean (SEM), with *n* being the number of cells tested, or clusters of cells where specified. Statistical comparisons were performed with nonparametric tests. When comparing two samples, we used the Mann-Whitney test for unpaired data and the Wilcoxon test for paired data. When comparing more than two samples, we used non-parametric ANOVA for repeated measures (Friedman test). The difference between proportions was assessed with Chi-square tests.

Results

OECs form a matrix surrounding OSN axons

Previous studies of the distribution and heterogeneity of OECs in tissue sections showed that S100B is a general marker of OECs in the mature OB (Au et al. 2002). Therefore, we analyzed labeled OECs in S100-GFP mice to study their structural relation with OSN axons. Fig.1A-A‴ shows that GFP was strongly expressed by cells in the olfactory nerve layer (ONL) and colocalized with brain lipid-binding protein (BLBP), expressed by OECs (Kurtz et al. 1994), with a slightly different subcellular localization. GFP was not expressed by meningeal cells on the surface of the OB, endothelial cells of the ONL, or periglomerular cells of the adjacent glomerular layer. GFP-labeled OECs displayed a matrix of fine processes extending from the cell body (Figs. 1A′ and 1B′). The OEC matrix formed small lacunae and immunohistochemistry for neural cell adhesion molecule (NCAM), strongly expressed in OSN axons, showed that the lacunae were occupied by OSN axons (Fig. 1B-B

‴). Similar results were obtained in tissue sections from non-transgenic CD-1 mice (Fig. S1A-A‴ and B-B‴).

OEC fine projections form an intricate matrix

The intricate matrix observed when all OECs were labeled with GFP led us to explore further the properties of individual OECs and their relation to neighboring OECs and axon bundles. To analyze the morphological and biophysical properties of individual OECs we performed whole-cell voltage clamp recordings of cells in the ONL, in acute OB slices. Because the biophysical properties of OECs are unknown, we used non-transgenic CD-1 mice in these studies (Figs. 2A-B).

During recording, OECs were filled with LY diffusing from the recording pipette to the cytoplasm of the patched OEC. Several projections running with different orientations were readily identified in LY-filled cells with an epifluorescence microscope (Fig. 2C). We often identified axon bundles parallel to the OEC processes, and a single OEC could be associated with neighboring axon bundles that differed in orientation (Figs. 2D-E).

To develop a higher resolution understanding of the morphology of LY-filled OECs, we scanned them with a confocal microscope and, performed quantitative 3D-reconstructions. OEC morphologies were complex (Fig. 3A-C and Suppl. video V1) and while variable among different OECs (Fig. S2), several common features emerged. First, the fine projections of OECs formed a matrix resembling that observed in S100-GFP mice (Fig. 3A). Second, OECs extended lamellar projections from the cell body, the longest projection averaging 43 ± 5 μm (Fig. 3B,D; n = 8). Third, OECs were elongated and flat cells; in a bounding box enclosing them, we could identify one largest dimension (length) and one smallest dimension (depth), which were significantly different (Fig. 3B,E). Thus, the spatial distribution of OEC processes tended to be restricted to a sublamina of the ONL. Fourth, surface area (4635 ± 537 μm^2) and volume (1157 ± 131 μm^3) showed a significant direct linear correlation (Fig. 3C, F-G; $p < 0.01$), indicating that a higher surface related to a larger size and not to a higher degree of elaboration in the fine projections (i.e. relatively constant surface/volume ratio of 3.56 ± 0.84 μm^{-1}).

We next asked whether the matrix formed by OEC fine projections had an ultrastructural correlate. We quantified the diameter of lacunae defined by OEC finer projections at the optical (Fig. 4A) and EM (Fig. 4B-C) levels. Ultrastructural analyses showed that most of the lacunae contained OSN axon bundles, confirming previous observations (Au et al. 2002;Doucette 1984;Valverde and Lopez-Mascaraque 1991). OEC lacunae had comparable diameters at the optical and EM levels (Fig. 4D); the most common value observed was in the 0.5-1.5 μm range for both approaches. Unexpectedly, we found lacunae with diameters larger than 6 μm and up to 15 μm at the EM level, not recognized at the optical level. Additionally, we did not detect lacunae of diameters below 1 μm at the optical level. This could be a consequence of light scattering in optical data, leading to an underestimation of larger lacunae and an inability to detect smaller lacunae.

Two populations of OECs with linear or non-linear current profiles

The morphological data showed a substantial diversity of OECs shape (Fig. S2). To ask if OECs were also heterogeneous in their electrophysiological properties, we recorded in whole cell configuration with a holding potential of -80 mV, near the resting potential expected for glial cells. To reveal voltage-dependent conductances, we stimulated OECs with a series of voltage steps at 20-mV intervals, from -160 to 120 mV. OECs displayed both hyperpolarization-activated inward currents and depolarization-activated outward currents. We found OECs with two distinct I/V profiles (Fig. 5A). A non-linear current

profile was found in 34% of patched OECs (n = 57 cells, 30 animals), owing to the activation of voltage-dependent outward currents between 0 and 20 mV, which inactivated slightly with time. A linear profile, with larger amplitude currents which inactivated slightly with strong depolarization, was found in 76% of OECs. We assessed linearity by fitting a straight line to the I/V curves (see Materials and methods). The linearity was significantly different for the two groups (Fig. 5B, Table 1). Linear OECs had lower Ri than non-linear cells, as expected from the larger amplitude of the currents measured. On the other hand, linear and non-linear OECs could not be distinguished based on their Vr (Fig. 5C, Table 1).

Dye coupling reveals a syncytial organization of OECs

In addition to differences in OEC biophysical properties, we found differences in the degree of dye-coupling. Of those OECs filled with LY, 47% were dye-coupled to neighboring cells (n = 30 cells, 21 animals). The cluster size of dye-coupled OECs ranged from 2 to 11 (mean = 5 ± 1; n = 14 clusters). Figure 6A-B shows a cluster of 11 OECs (see also Suppl. video V2). To analyze the structure of OEC clusters we performed 3D-reconstructions similar to those done for individual OECs (Fig. 6C and Suppl. Video V2). We asked whether an OEC was coupled to all its neighbors or, alternatively, if there were domains of preferentially coupled OECs. To analyze this, we considered clusters of 5 cells or more. We defined a north and south hemisphere for each cluster (see Materials and methods and Fig. 6D) and evaluated the number of dye-coupled cells in each hemisphere. Because asymmetries in the distribution of dye-coupled cells could be due to asymmetry of neighbors available for coupling, we evaluated the number of nuclei in each hemisphere as well. Figure 6E shows a plot of the proportion of dye-coupled cells in the northern hemisphere vs. the proportion of nuclei in the same hemisphere. If all asymmetries in the distribution of dye coupled cells were due to asymmetries in the distribution of neighbors, all points should fall on the slope = 1 line. However, most of the data are above this line (slope = 1.42), indicating that asymmetries in the distribution of coupled cells are larger than what is expected from asymmetry in the availability of potential targets.

To obtain information regarding the location of coupling sites, we asked whether the strength of dye-coupling depended on the distance between the recorded and coupled cell bodies. Figure 6F shows a poor correlation between dye intensity measured at the cell body of coupled cells vs. distance to the injected cell body. The brightest OEC cell bodies were typically close to the injected cell (< 30 μm). However, a substantial proportion of OEC somata located close to the injected cell (56 ± 8%) showed low intensity fluorescence (lower than 0.25). These data indicate that coupling sites between OECs were not primarily somatic.

We previously showed a sublaminar organization of the ONL with an inner (deep) and outer (more superficial) layers based on the differential distribution of molecular markers (Au et al. 2002). To address whether OEC properties varied depending on their depth in the ONL, we classified OECs in deep, intermediate or superficial (see Materials and methods). We found no significant differences among these groups regarding the diameter of lacunae the proportion of linear cells versus non-linear cells or the size of dye coupled clusters (not shown).

OEC current profiles are shaped by connectivity

We then asked whether the likelihood and/or strength of dye-coupling was related to the type of current profile exhibited by an OEC (linear vs. non-linear). Figure 7A shows that non-linear cells were less commonly dye-coupled (23%) than linear cells (67%) ($p < 0.05$). Furthermore, clusters in which the recorded cell was non-linear had fewer cells than clusters in which the recorded cell was linear (Fig. 7B). Interestingly, for the few cases in which

non-linear cells were dye-coupled, the cluster had only the recorded cell plus one additional cell.

The lower Ri of linear OECs (Fig. 5C), together with the higher probability of significant dye-coupling (Fig. 7A-B) strongly suggested that they were gap-junction coupled. To address this question we performed paired recordings of neighboring OECs. Figure 7C shows representative recordings of one pair of electrically coupled OECs. When a series of voltage steps was applied in either cell, large currents with a linear profile were recorded. In addition, outward currents in the stimulated cell corresponded with inward currents in the non-stimulated cell, and vice versa, as expected with a direct flow of current between the cells. When the non-stimulated cell was switched to current clamp mode, we measured changes in membrane potential which represented 11 ± 2% of the changes imposed to the stimulated cell, indicating a poor space clamp at the cell bodies of coupled OECs (n = 4, not shown).

When coupled OECs were exposed to the gap junction blocker MFA (Fig. 7D) we observed that: 1) All currents in the stimulated cell were significantly reduced, increasing Ri (Table 1), indicating that previously available paths for current flow were blocked; 2) Currents recorded in the non-stimulated cell disappeared, suggesting that current could no longer flow from cell to cell; 3) The profiles of stimulated cells became less linear, as indicated by a significant reduction in r^2, the correlation coefficient used to measure linearity of I/V curves (see Materials and methods and Table 1); and 4) The Vr of OECs was not affected (Table 1). These results strongly suggested that linear and non-linear OECs are not different cell types, but rather the same type in a gap junction-connected or disconnected mode, respectively. The average maximum current elicited in control conditions by a 120-mV voltage command was 7.3 ± 1.1 nA and was significantly reduced to 2.6 ± 0.6 nA in MFA ($p < 0.005$; n = 8 cells, 4 animals), a 66 ± 5% block (Fig. 7E), indicating that a gap junction conductance represented a large proportion of the total current in linear OECs. The gap junction conductance between the two connected cells (see Materials and methods) was significantly reduced from 5.3 ± 1.9 nS in control to 0.8 ± 0.3 nS in MFA ($p < 0.05$; n = 4 cell pairs, 3 animals). The MFA-sensitive current had a linear I/V curve with a reversal potential of -63 ± 5 mV (Fig. 7F). The effects of MFA on linear OECs were only partially washed in juvenile tissue, but were almost completely washed in neonatal tissue (Fig. S3A, n = 2). Consistently, MFA had little effect on non-linear OECs (Fig. S3B, n = 3), supporting our view that these cells were already uncoupled. These observations led us to conclude that the biophysical diversity observed in OECs is determined by gap junction connectivity.

Connexin expression and gap junctions in OECs

We then studied the distribution of glial connexin proteins (Cxs), candidate mediators of electrical coupling, in the ONL and individual OECs. We looked for colocalization of GFP (in the S100-GFP mouse OB) with immunoreactivity to three different connexins expressed in glial cells: Cx43, Cx32 and Cx26. We found no immunoreactivity to Cx32 or Cx26 in OECs (not shown). Conversely, Cx43 was highly enriched in the ONL (Fig. 8A-B). Cx43 immunoreactivity organized in small clusters (average volume: 0.57 ± 0.13 μm^3; n = 6 animals; 1,532 clusters) which aligned with fine OEC projections in the ONL (Fig. 8A′-A‴,C) and were scattered throughout the surface of OECs up to the tips of far-reaching projections (Fig. 8D). A similar distribution of Cx43 immunoreactivity was observed in non-trangenic CD-1 mice (Fig. S1C-C‴). At the EM level, we found the ultrastructural correlate of gap junction specializations cut in cross-section, in apposed glial profiles of the ONL (Fig. 8E). The average length of these specializations was 1.3 ± 0.2 μm (n = 10 connections, 3 animals). These data suggest that Cx43 is a likely mediator of gap junction coupling in OECs.

Discussion

We establish for the first time the detailed morphological features of OECs, at the level of both the confocal and electron microscope, and demonstrate that clusters of gap junction coupled OECs can form a syncytium that is a determinant of OEC biophysical properties.

Morphologically unique glial cells

OECs were previously assessed at the light microscopy level using Golgi stains (Valverde and Lopez-Mascaraque 1991) and in tissue prepared for EM (Au et al. 2002; Doucette 1984). Nevertheless, we show the detailed complex matrix formed by single OECs, which has not been previously described for any type of glial cell. OECs are in an ideal position to influence axons, as they pass through lacunae of the linearly oriented OEC projections, via apposed interactions and diffusible factors, since OSN axons on the outer perimeter of a fascicle are in close contact with OECs, while others within the interior of a fascicle are not (Johansson et al. 2005; Kafitz and Greer 1999; Runyan and Phelps 2009; Sonigra et al. 1999; Woodhall et al. 2001). The OEC complex morphology prevented us from using standard methods to quantify size and structure. However, we developed analyses that may apply to other complex cells. Additionally, we introduced the S100-GFP mice as a tool for labeling OECs, which together with labeling OSN axon subpopulations opens a path to study neuron-glia interactions in whole preparations.

Syncytial organization of OECs

Functionally significant gap junction coupling among OECs was not previously shown, but may have a profound impact on the role of OECs in supporting/guiding OSN axons. Prior ultrastructural analyses and connexin expression, both *in vitro* and *in vivo*, suggested that gap junction coupling occurs between OECs (Barnett et al. 2001; Blinder et al. 2003; Mack and Wolburg 1986; Rash et al. 2005). There is no evidence of the existence of gap junctions between OECs and OSN axons (Blinder et al. 2003), supported by the lack of structures morphologically compatible with axons dye coupled to LY-filled OECs. Dye coupling was shown in immortalized OECs *in vitro* (Barnett et al, 2001). However, because OECs dramatically change phenotype depending on culture conditions (Alexander et al. 2002; Franceschini and Barnett 1996; Vincent et al. 2003), a definitive evaluation of gap junction properties cannot rest solely on *in vitro* analyses. We show the first functional demonstration of gap junction coupling of OECs *in situ*, confirmed pharmacologically. Moreover, we show that coupling occurs among OECs that we speculate are functionally related. While proximity of OEC somata was a predictor of coupling, in many cases proximal OECs were not coupled, showing that neighbor:neighbor relations in the ONL can be selective. One factor to explain preferential coupling is the non-radial symmetry of OECs, which would bias the possible interactions towards where the cell projections extend. The finding that proximal cell bodies are not always strongly dye coupled supports this view, suggesting that at least some coupling sites are in OEC processes. In addition, weakly stained OEC somata close to the injected cell may have been labeled indirectly through an intermediary cell. These dye-coupling experiments suggest that one OEC may be preferentially coupled to a subset of its neighbors forming OEC subdomains with the potential to affect specific axon fascicles.

Linearity of glial I/V curves

Linear current profiles were reported for other glial cells (Akopian et al. 1997; Chvatal et al. 1995; D'Ambrosio et al. 1998; Schools et al. 2006; Serrano et al. 2008; Steinhauser et al. 1992; Zhou and Kimelberg 2000). It is controversial whether linear behavior reflects intrinsic properties of the cells or results from profuse gap junction coupling. Indirect evidence has been provided for both situations in different glial cells (see above) and could

also be artifactual (Bordey and Sontheimer 1998). We provide the first direct demonstration that gap junction coupling explains the linear behavior in OECs, which is lost upon uncoupling. We understand this effect as a combination of cell properties and recording strategy. In an uncoupled cell the voltage commands are expected to reach the activation threshold of voltage-dependent conductances effectively producing a non-linear current profile. Alternatively, when coupled a relatively large gap junction conductance appears in parallel with other membrane conductances (Fig. S4). Gap junctions with weak voltage-dependence, will add a significant linear component to the current profile, masking nonlinearities of intrinsic voltage-dependent conductances. In cell clusters, the membrane of coupled cells would be poorly voltage clamped, explaining why a non-linear profile of large amplitude currents is not observed. Unexpectedly, the capacitance of linear and non-linear cells did not differ (Table 1). Further, there was no change in capacitance when linear cells were uncoupled pharmacologically (Table 1). One possible explanation is that capacitance estimates are inaccurate for cell clusters with poor space clamp, given that capacitive transients on which the estimates are based are not pronounced and do not fit well to a single exponential function. A similar phenomenon and interpretation was reported for gap junction coupled fibroblasts in culture, in which capacitance measurements became unreliable for cell clusters larger than 10 cells (de Roos et al. 1996).

Whether linear (coupled) and non-linear (uncoupled) cells are different maturational stages of OECs or interchangeable functional states remains to be further studied, however, the occasional spontaneous switch from linear to non-linear profiles (not shown) favors the latter. Interestingly, we identified Cx43 clusters colocalizing with OECs which were not dye-coupled (Fig. 8D), suggesting that uncoupled cells did not lack the connections; rather, uncoupled cells have gap junctions in a non-functional state.

The dramatic change in biophysical properties produced in OECs by the gap junction blocker MFA is in striking contrast to that reported for hippocampal astrocytes, in which MFA reduces dye coupling but does not significantly alter the current profile (Schools et al. 2006). This could reflect a differential distribution of gap junction sites, with those in OECs less electrically isolated from the cell body than in astrocytes.

Lucifer yellow fills indicate that 47% of OECs display dye coupling. Our electrophysiological data suggest that 76% of OECs (linear OECs) are electrically and thus gap junction coupled. This discrepancy could reflect the sensitivity limit of dye coupling to detect gap junction coupling (Peinado et al. 2003). Alternatively, mechanisms additional to gap junction coupling could explain the linear current profile in some of the OECs. However, the latter is not supported by the fact that the linearity of the current profile of all linear OECs treated with MFA was reduced.

Physiological relevance

Gap junction coupling in glial cells has been postulated to participate in the homeostasis of extracellular fluids, in particular, K^+ buffering (Leis et al. 2005; Simard and Nedergaard 2004; Wang and Bordey 2008; Menichella et al. 2006). Whether gap junctions in OECs play a role in K^+ buffering in the ONL requires further study but could constitute a mechanism to modulate OSN axon excitability (Wallraff et al. 2006). Interestingly, preventing gap junction coupling in hippocampal astrocytes interferes with the trafficking of energy metabolites necessary to sustain glutamatergic synaptic transmission among neurons (Rouach et al. 2008). Ultrastructural analyses of the ONL indicate that OECs are not in close proximity to synaptic sites (Doucette 1984). However, our results open the question about a possible role of OEC networks in modulating neurotransmitter release from growing OSN axons or a possible paracrine effect on synaptic transmission at glomeruli, where OSN axons make synapses after dissociating from OECs.

In light of the properties of OECs as promoters of axon growth, we propose an additional possible role of gap junctions in these cells. At least part of the growth promoting effects of OECs involves the release of soluble factors (Kafitz and Greer 1999; Runyan and Phelps 2009; Woodhall et al. 2001). The signals regulating release are not fully known, however calcium transients in response to neurotransmitter release from OSN axons could be involved (Rieger et al. 2007); altering calcium signaling in OECs makes them less efficient promoters of neurite growth *in vitro* (Hayat et al. 2003). Gap junction coupling participates in the propagation of intercellular calcium waves in astrocytes during development (Parri et al. 2001; Weissman et al. 2004) and in pathological conditions (Kuchibhotla et al. 2009; Peters et al. 2003), constituting a network with effects on neuronal function in the relatively long range (Fiacco and McCarthy 2006; Scemes and Giaume 2006). Our data demonstrate that OECs are equipped with functional gap junctions with the potential to propagate signals through the flow of second messengers to neighboring OECs. We can consider two possibilities in which gap junction-coupled OECs could modulate axon growth (see Fig. S5): 1) OECs form widespread networks that are recruited to release neurotrophins, producing a generally permissive environment for axon growth in the ONL; 2) OECs are recruited to form small domains to coordinately release growth factors creating local gradients of neurotrophins. Although our dye coupling experiments favor the second view, the likelihood of these possibilities will depend on the permeability of gap junctions to the second messengers in play.

These models add a new level of complexity to the current view of possible mechanisms that may mediate effects of OECs on axon growth and sorting. In addition to glia-axon contacts and glial release of neurotrophins, glia-glia coupling can be considered as a potential factor modulating OEC functions.

Supplementary Material

Refer to Web version on PubMed Central for supplementary material.

Acknowledgments

We are grateful to Dr. Wesley Thompson for the S100-GFP mice, to Dr. Anne Williamson for advice and resources, to Dolores Montoya and Christine Kaliszewski for expert technical assistance and to Dr. M. Rafael Pagani, Dr. M. Eugenia Chiappe and all members of the Greer lab for invaluable discussions and critical reading of the manuscript. Supported by NIH DC007880, DC006972, and DC000210.

References

Akopian G, Kuprijanova E, Kressin K, Steinhuser C. Analysis of ion channel expression by astrocytes in red nucleus brain stem slices of the rat. Glia. 1997; 19(3):234–46. [PubMed: 9063730]

Alexander CL, Fitzgerald UF, Barnett SC. Identification of growth factors that promote long-term proliferation of olfactory ensheathing cells and modulate their antigenic phenotype. Glia. 2002; 37(4):349–64. [PubMed: 11870874]

Altman J. Autoradiographic and histological studies of postnatal neurogenesis. IV. Cell proliferation and migration in the anterior forebrain, with special reference to persisting neurogenesis in the olfactory bulb. J Comp Neurol. 1969; 137(4):433–57. [PubMed: 5361244]

Au WW, Treloar HB, Greer CA. Sublaminar organization of the mouse olfactory bulb nerve layer. J Comp Neurol. 2002; 446(1):68–80. [PubMed: 11920721]

Barnett SC, Riddell JS. Olfactory ensheathing cell transplantation as a strategy for spinal cord repair--what can it achieve? Nat Clin Pract Neurol. 2007; 3(3):152–61. [PubMed: 17342191]

Barnett SC, Thompson RJ, Lakatos A, Pitts J. Gap junctional communication and connexin expression in cultured olfactory ensheathing cells. J Neurosci Res. 2001; 65(6):520–8. [PubMed: 11550220]

Bartolomei JC, Greer CA. Olfactory ensheathing cells: bridging the gap in spinal cord injury. Neurosurgery. 2000; 47(5):1057–69. [PubMed: 11063098]

Blinder KJ, Pumplin DW, Paul DL, Keller A. Intercellular interactions in the mammalian olfactory nerve. J Comp Neurol. 2003; 466(2):230–9. [PubMed: 14528450]

Bordey A, Sontheimer H. Passive glial cells, fact or artifact? J Membr Biol. 1998; 166(3):213–22. [PubMed: 9843595]

Bordey A, Sontheimer H. Ion channel expression by astrocytes in situ: comparison of different CNS regions. Glia. 2000; 30(1):27–38. [PubMed: 10696142]

Brightman MW, Reese TS. Junctions between intimately apposed cell membranes in the vertebrate brain. J Cell Biol. 1969; 40(3):648–77. [PubMed: 5765759]

Cafferty W, Yang S, Duffy P, Li S, Strittmatter S. Functional axonal regeneration through astrocytic scar genetically modified to digest chondroitin sulfate proteoglycans. J Neurosci. 2007; 27(9): 2176–85. [PubMed: 17329414]

Caggiano M, Kauer JS, Hunter DD. Globose basal cells are neuronal progenitors in the olfactory epithelium: a lineage analysis using a replication-incompetent retrovirus. Neuron. 1994; 13(2): 339–52. [PubMed: 8060615]

Carleton A, Petreanu L, Lansford R, Alvarez-Buylla A, Lledo P. Becoming a new neuron in the adult olfactory bulb. Nat Neurosci. 2003; 6(5):507–18. [PubMed: 12704391]

Chvatal A, Pastor A, Mauch M, Sykova E, Kettenmann H. Distinct populations of identified glial cells in the developing rat spinal cord slice: ion channel properties and cell morphology. Eur J Neurosci. 1995; 7(1):129–42. [PubMed: 7536092]

D'Ambrosio R, Wenzel J, Schwartzkroin PA, McKhann GM 2nd, Janigro D. Functional specialization and topographic segregation of hippocampal astrocytes. J Neurosci. 1998; 18(12):4425–38. [PubMed: 9614220]

de Roos AD, van Zoelen EJ, Theuvenet AP. Determination of gap junctional intercellular communication by capacitance measurements. Pflügers Arch. 1996; 431(4):556–563.

Doucette JR. The glial cells in the nerve fiber layer of the rat olfactory bulb. Anat Rec. 1984; 210(2): 385–91. [PubMed: 6507903]

Doucette R. Glial influences on axonal growth in the primary olfactory system. Glia. 1990; 3(6):433–49. [PubMed: 2148546]

Doucette R. Glial cells in the nerve fiber layer of the main olfactory bulb of embryonic and adult mammals. Microsc Res Tech. 1993; 24(2):113–30. [PubMed: 8457724]

Fiacco T, McCarthy K. Astrocyte calcium elevations: properties, propagation, and effects on brain signaling. Glia. 2006; 54(7):676–90. [PubMed: 17006896]

Franceschini IA, Barnett SC. Low-affinity NGF-receptor and E-N-CAM expression define two types of olfactory nerve ensheathing cells that share a common lineage. Dev Biol. 1996; 173(1):327–43. [PubMed: 8575633]

Gogos J, Osborne J, Nemes A, Mendelsohn M, Axel R. Genetic ablation and restoration of the olfactory topographic map. Cell. 2000; 103(4):609–20. [PubMed: 11106731]

Graziadei PP, Graziadei GA. Neurogenesis and neuron regeneration in the olfactory system of mammals. I. Morphological aspects of differentiation and structural organization of the olfactory sensory neurons. J Neurocytol. 1979; 8(1):1–18. [PubMed: 438867]

Harding JW, Wright JW. Reversible effects of olfactory nerve section on behavior and biochemistry in mice. Brain Res Bull. 1979; 4(1):17–22. [PubMed: 89004]

Hayat S, Thomas A, Afshar F, Sonigra R, Wigley C. Manipulation of olfactory ensheathing cell signaling mechanisms: effects on their support for neurite regrowth from adult CNS neurons in coculture. Glia. 2003; 44(3):232–41. [PubMed: 14603464]

Johansson S, Lee IH, Olson L, Spenger C. Olfactory ensheathing glial co-grafts improve functional recovery in rats with 6-OHDA lesions. Brain. 2005; 128(Pt 12):2961–76. [PubMed: 16251218]

Kafitz KW, Greer CA. Olfactory ensheathing cells promote neurite extension from embryonic olfactory receptor cells in vitro. Glia. 1999; 25(2):99–110. [PubMed: 9890625]

Kuchibhotla K, Lattarulo C, Hyman B, Bacskai B. Synchronous hyperactivity and intercellular calcium waves in astrocytes in Alzheimer mice. Science. 2009; 323(5918):1211–5. [PubMed: 19251629]

Kurtz A, Zimmer A, Schnutgen F, Bruning G, Spener F, Muller T. The expression pattern of a novel gene encoding brain-fatty acid binding protein correlates with neuronal and glial cell development. Development. 1994; 120(9):2637–49. [PubMed: 7956838]

Leis JA, Bekar LK, Walz W. Potassium homeostasis in the ischemic brain. Glia. 2005; 50(4):407–16. [PubMed: 15846795]

Li Y, Field PM, Raisman G. Regeneration of adult rat corticospinal axons induced by transplanted olfactory ensheathing cells. J Neurosci. 1998; 18(24):10514–24. [PubMed: 9852589]

Liesi P. Laminin-immunoreactive glia distinguish regenerative adult CNS systems from non-regenerative ones. EMBO J. 1985; 4(10):2505–11. [PubMed: 3902469]

Mack A, Wolburg H. Heterogeneity of glial membranes in the rat olfactory system as revealed by freeze-fracturing. Neurosci Lett. 1986; 65(1):17–22. [PubMed: 3703378]

Menichella DM, Majdan M, Awatramani R, Goodenough DA, Sirkowski E, Scherer SS, Paul DL. Genetic and physiological evidence that oligodendrocyte gap junctions contribute to spatial buffering of potassium released during neuronal activity. J Neurosci. 2006; 26(43):10984–91. [PubMed: 17065440]

Mombaerts P, Wang F, Dulac C, Chao SK, Nemes A, Mendelsohn M, Edmondson J, Axel R. Visualizing an olfactory sensory map. Cell. 1996; 87(4):675–86. [PubMed: 8929536]

Montague A, Greer C. Differential distribution of ionotropic glutamate receptor subunits in the rat olfactory bulb. J Comp Neurol. 1999; 405(2):233–46. [PubMed: 10023812]

Parri H, Gould T, Crunelli V. Spontaneous astrocytic Ca2+ oscillations in situ drive NMDAR-mediated neuronal excitation. Nat Neurosci. 2001; 4(8):803–12. [PubMed: 11477426]

Peinado A, Yuste R, Katz LC. Extensive dye coupling between rat neocortical neurons during the period of circuit formation. Neuron. 2003; 10(1):103–14. [PubMed: 8427699]

Peters O, Schipke C, Hashimoto Y, Kettenmann H. Different mechanisms promote astrocyte Ca2+ waves and spreading depression in the mouse neocortex. J Neurosci. 2003; 23(30):9888–96. [PubMed: 14586018]

Raisman G, Li Y. Repair of neural pathways by olfactory ensheathing cells. Nat Rev Neurosci. 2007; 8(4):312–9. [PubMed: 17342173]

Rash JE, Davidson KG, Kamasawa N, Yasumura T, Kamasawa M, Zhang C, Michaels R, Restrepo D, Ottersen OP, Olson CO, et al. Ultrastructural localization of connexins (Cx36, Cx43, Cx45), glutamate receptors and aquaporin-4 in rodent olfactory mucosa, olfactory nerve and olfactory bulb. J Neurocytol. 2005; 34(3-5):307–41. [PubMed: 16841170]

Ressler KJ, Sullivan SL, Buck LB. Information coding in the olfactory system: evidence for a stereotyped and highly organized epitope map in the olfactory bulb. Cell. 1994; 79(7):1245–55. [PubMed: 7528109]

Rieger A, Deitmer J, Lohr C. Axon-glia communication evokes calcium signaling in olfactory ensheathing cells of the developing olfactory bulb. Glia. 2007; 55(4):352–9. [PubMed: 17136772]

Rouach N, Koulakoff A, Abudara V, Willecke K, Giaume C. Astroglial metabolic networks sustain hippocampal synaptic transmission. Science. 2008; 322(5907):1551–5. [PubMed: 19056987]

Runyan SA, Phelps PE. Mouse olfactory ensheathing glia enhance axon outgrowth on a myelin substrate in vitro. Exp Neurol. 2009; 216(1):95–104. [PubMed: 19100263]

Scemes E, Giaume C. Astrocyte calcium waves: what they are and what they do. Glia. 2006; 54(7): 716–25. [PubMed: 17006900]

Schools GP, Zhou M, Kimelberg HK. Development of gap junctions in hippocampal astrocytes: evidence that whole cell electrophysiological phenotype is an intrinsic property of the individual cell. J Neurophysiol. 2006; 96(3):1383–92. [PubMed: 16775204]

Schwab ME. Repairing the injured spinal cord. Science. 2002; 295(5557):1029–31. [PubMed: 11834824]

Serrano A, Robitaille R, Lacaille JC. Differential NMDA-dependent activation of glial cells in mouse hippocampus. Glia. 2008; 56(15):1648–63. [PubMed: 18618659]

Simard M, Nedergaard M. The neurobiology of glia in the context of water and ion homeostasis. Neuroscience. 2004; 129(4):877–96. [PubMed: 15561405]

Sonigra RJ, Brighton PC, Jacoby J, Hall S, Wigley CB. Adult rat olfactory nerve ensheathing cells are effective promoters of adult central nervous system neurite outgrowth in coculture. Glia. 1999; 25(3):256–69. [PubMed: 9932872]

Steinhauser C, Berger T, Frotscher M, Kettenmann H. Heterogeneity in the Membrane Current Pattern of Identified Glial Cells in the Hippocampal Slice. Eur J Neurosci. 1992; 4(6):472–484. [PubMed: 12106333]

Treloar H, Feinstein P, Mombaerts P, Greer C. Specificity of glomerular targeting by olfactory sensory axons. J Neurosci. 2002; 22(7):2469–77. [PubMed: 11923411]

Valverde F, Lopez-Mascaraque L. Neuroglial arrangements in the olfactory glomeruli of the hedgehog. J Comp Neurol. 1991; 307(4):658–74. [PubMed: 1714466]

Vassar R, Chao SK, Sitcheran R, Nunez JM, Vosshall LB, Axel R. Topographic organization of sensory projections to the olfactory bulb. Cell. 1994; 79(6):981–91. [PubMed: 8001145]

Vincent AJ, Taylor JM, Choi-Lundberg DL, West AK, Chuah MI. Genetic expression profile of olfactory ensheathing cells is distinct from that of Schwann cells and astrocytes. Glia. 2005; 51(2): 132–47. [PubMed: 15789429]

Vincent AJ, West AK, Chuah MI. Morphological plasticity of olfactory ensheathing cells is regulated by cAMP and endothelin-1. Glia. 2003; 41(4):393–403. [PubMed: 12555206]

Wallraff A, Kohling R, Heinemann U, Theis M, Willecke K, Steinhauser C. The impact of astrocytic gap junctional coupling on potassium buffering in the hippocampus. J Neurosci. 2006; 26(20): 5438–47. [PubMed: 16707796]

Wang D, Bordey A. The astrocyte odyssey. Prog Neurobiol. 2008; 86(4):342–67. [PubMed: 18948166]

Wang D, Krueger D, Bordey A. Biophysical properties and ionic signature of neuronal progenitors of the postnatal subventricular zone in situ. J Neurophysiol. 2003a; 90(4):2291–302. [PubMed: 12801891]

Wang D, Krueger D, Bordey A. GABA depolarizes neuronal progenitors of the postnatal subventricular zone via GABAA receptor activation. J Physiol. 2003b; 550(Pt 3):785–800. [PubMed: 12807990]

Weissman T, Riquelme P, Ivic L, Flint A, Kriegstein A. Calcium waves propagate through radial glial cells and modulate proliferation in the developing neocortex. Neuron. 2004; 43(5):647–61. [PubMed: 15339647]

Whitman M, Greer C. Adult-generated neurons exhibit diverse developmental fates. Dev Neurobiol. 2007a; 67(8):1079–93. [PubMed: 17565001]

Whitman M, Greer C. Synaptic integration of adult-generated olfactory bulb granule cells: basal axodendritic centrifugal input precedes apical dendrodendritic local circuits. J Neurosci. 2007b; 27(37):9951–61. [PubMed: 17855609]

Woodhall E, West AK, Chuah MI. Cultured olfactory ensheathing cells express nerve growth factor, brain-derived neurotrophic factor, glia cell line-derived neurotrophic factor and their receptors. Brain Res Mol Brain Res. 2001; 88(1-2):203–13. [PubMed: 11295250]

Zhao C, Deng W, Gage FH. Mechanisms and functional implications of adult neurogenesis. Cell. 2008; 132(4):645–60. [PubMed: 18295581]

Zhou M, Kimelberg HK. Freshly isolated astrocytes from rat hippocampus show two distinct current patterns and different [K(+)](o) uptake capabilities. J Neurophysiol. 2000; 84(6):2746–57. [PubMed: 11110805]

Zuo Y, Lubischer J, Kang H, Tian L, Mikesh M, Marks A, Scofield V, Maika S, Newman C, Krieg P, et al. Fluorescent proteins expressed in mouse transgenic lines mark subsets of glia, neurons, macrophages, and dendritic cells for vital examination. J Neurosci. 2004; 24(49):10999–1009. [PubMed: 15590915]

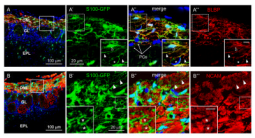

Figure 1.

OECs are closely associated with axons in the ONL. Immunohistochemistry in OB sections of S100-GFP mice (P26). ***A*** and ***B,*** OB layers indicating the locations shown at higher magnification to the right (square). ONL: Olfactory nerve layer; GL: glomerular layer; EPL: external plexiform layer. Nuclei were stained with DRAQ5. ***A′-A‴,*** Colocalization of GFP (green) with BLBP (red) in OECs. Insets: higher magnifications of the area inside the dashed square; Scale bar = 5 μm. Filled arrowheads: OEC fine processes; open arrowhead: OEC cell body; asterisk: next to endothelial cell. PGs: Periglomerular cells. ***B′-B‴,*** Immunoreactivity for NCAM, a marker for OSN axons (red), is in the lacunae (asterisks) defined by the matrix of fine OEC processes (arrowheads).

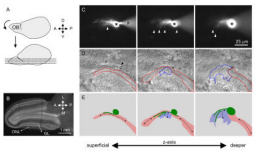

Figure 2.

OEC projections align with neighboring axon bundles. ***A***, Slicing procedure for horizontal slices; the anteroventral surface of the brain was glued to a vibratome stage and sliced. ***B***, A horizontal OB slice, fixed and stained for nuclei with DRAQ5. Dashed line: limit between the olfactory nerve layer (ONL), where cells were recorded, and the glomerular layer (GL). ***C***, Fluorescence images showing a LY-filled OEC at three different depths in the tissue slice (superficial to the left). Asterisk: cell body; white arrowheads: projections; 'p': recording pipette. ***D***, DIC image of the areas in ***C***. Black arrowhead: pipette tip. Axon bundles delineated with red and blue (dashed lines) run in nearly perpendicular directions. ***E***, Cartoons of the outlined cell body and projections in ***C*** (green) and areas in ***D***. Black arrows: orientation of axon bundles.

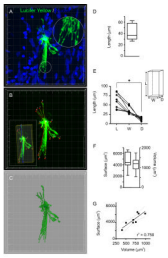

Figure 3.

OECs are elongated cells with fine projections forming a matrix. ***A,*** Volume 3D-reconstruction of a LY-filled OEC (Grid: 5 μm). Nuclei were stained with DRAQ5. Inset: matrix of lamellar projections (dashed circle). ***B,*** Points (red) defined to estimate the length of OEC projections. Inset: the OEC main axis is in blue and a bounding box enclosing the cell is in yellow (see Materials and methods). ***C,*** Isosurface rendering using the green channel. The blue channel was used to generate a contour surface of the nucleus. ***D,*** Length of the longest segment from the cell body to the tip of lamellae, as indicated in ***B*** (n = 8). ***E,*** Length, width and depth of the bounding boxes enclosing each OEC, as shown in ***B*** (inset) (n = 8). * $p < 0.001$ (Friedman test). ***F,*** Surface and volume of isosurface renderings as the one shown in ***C*** (n = 8). ***G,*** Surface vs. volume plot (full line: linear fit; broken lines: 95% confidence interval; $r^2 = 0.75$; n = 8).

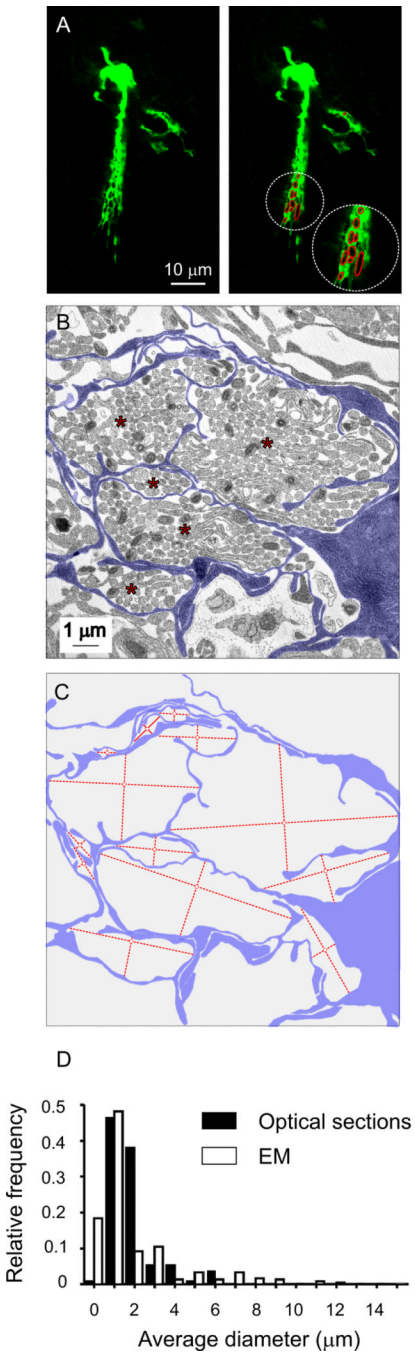

Figure 4.

Ultrastructural correlate of the matrix formed by dye-filled OECs. ***A,*** Single optical section of a LY-filled OEC. Right panel: lacunae defined by fine interdigitations fitted to elliptical regions of interest (red) used for quantification (see Materials and methods). ***B,*** Electron micrograph of the olfactory nerve layer. Blue: contoured glial processes; red asterisks: axon bundles surrounded by glial projections. ***C,*** The same contour as in ***B*** showing the strategy used to quantify the average diameter of lacunae at the EM level. Maximum and minimum diameters are indicated with perpendicular red lines. ***D,*** Histogram showing the average diameter of lacunae measured in confocal single optical sections (black bars) or in electron micrographs (white bars).

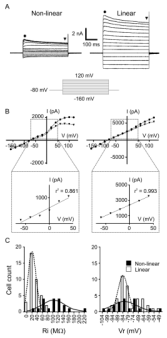

Figure 5.

Current profiles in OECs. ***A,*** Representative recordings of an OEC with non-linear (left) or linear (right) current profiles in response to a series of 20-mV, 400-ms voltage steps; holding potential: -80 mV. The series of 15 steps started at -160 mV (schematized below). ***B,*** I/V curves of the recordings in ***A***, with currents measured at the times indicated with symbols. The range indicated by the dashed rectangle was fitted to a straight line (expanded below). ***C,*** Histograms of Ri (left) and Vr (right) from cells with non-linear (black bars) and linear (white bars) cells. Bell-shape curves: Gaussian fits to the non-linear cell (full line) or linear cell (broken line) data.

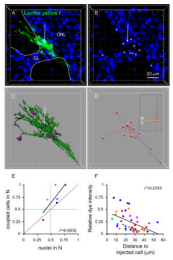

Figure 6.

Dye coupling in OECs. ***A,*** Cluster of 11 dye-coupled OECs (green) with nuclei stained with DRAQ5 (blue). Grid: 10 μm. Arrow in ***A*** and ***B***: recorded cell. GL: glomerular layer. Dashed lines delineate the glomeruli. Asterisks in ***B:*** nuclei of dye-coupled cells. ***C,*** Isosurface rendering of the green channel. The nuclear staining (blue channel) was used to generate contour surfaces of the nuclei of the injected cell (blue) and dye-coupled cells (purple). ***D,*** Segments: linear distance between the cell body of the injected cell and those of the coupled cells (red) and cluster main axis (blue, see Materials and methods). Inset: the same cluster oriented with north (N) pointing up and the equator indicated (dashed yellow line). ***E,*** Proportion of coupled cells vs. the proportion of nuclei in the northern hemisphere (N). Each point is a different cluster. The vertical and horizontal dotted lines correspond to symmetrical distribution of nuclei and coupled cells on both sides of the equator, respectively. The dashed line corresponds to slope=1. ***F,*** Dye intensity at the cell bodies of coupled cells vs. the linear distance to the injected cell. Each point is a different cell and each color is a different cluster, matching ***E***. The lines in ***E*** and ***F*** are linear regressions.

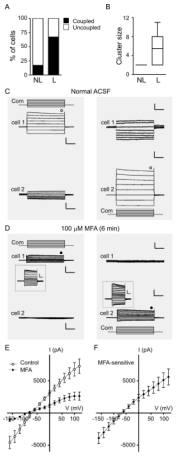

Figure 7.

Gap junction coupling in OECs. ***A,*** Percentage of the total recorded non-linear (NL) or linear (L) cells dye-coupled to other cells (black column). The complementary percentage of uncoupled cells is shown in white. ***B,*** Cluster size (number of stained cells) associated with non-linear (NL) or linear (L) cells. ***C,*** Representative recordings of membrane currents of two OECs recorded simultaneously (cell 1 at the top and cell 2 at the bottom). Left panel: responses of the two cells when cell 1 was stimulated with a series of 20-mV voltage steps; holding potential: -80 mV. The series of 13 steps started at -160 mV. Right panel: responses when the same stimulation protocol was applied only to cell 2. The command voltage (Com) is schematized above (cell 1) or below (cell 2) the traces of the stimulated cell. Scale bars: 2 nA (stimulated cell) or 100 pA (non-stimulated cell), and 100 ms. ***D,*** The same cells and experimental protocol as in ***C***, during bath-application of the gap-junction blocker meclofenamic acid (MFA, 100μM). Scale bars: same as in D; inset scale bars = 0.5 nA, 100 ms. ***E,*** Average I/V curves (n = 8) of OECs subjected to the voltage steps in control conditions (open circles) and after application of MFA (filled circles). The current amplitude was measured at the time indicated with symbols in ***C*** and ***D. F,*** Average I/V curve of the MFA-sensitive current (n = 8). Error bars represent SEM.

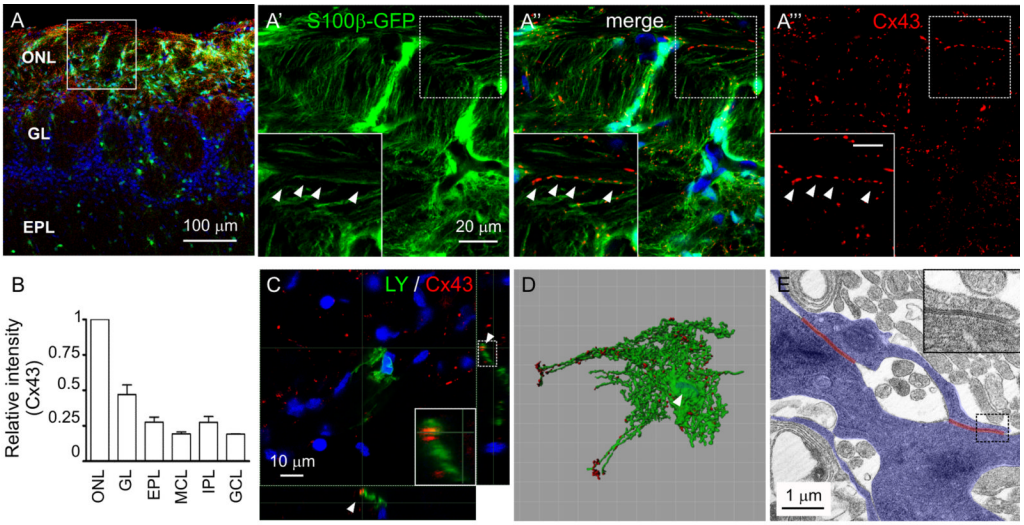

Figure 8.

Expression of Connexin 43 in OECs. ***A,*** Immunohistochemistry in an OB section of S100-GFP mice (p26). Low magnification of the OB layers indicating the locations where the images were acquired (square). Nuclei were stained with DRAQ5. ***A′-A‴,*** Clusters of Cx43 immunoreactivity (red) colocalize with GFP-labeled fine projections of OECs (arrowheads). Insets: higher magnifications of the area inside the dashed square; Scale bar = 5 μm. ***B,*** Average intensity of Cx43 immunoreactivity in each layer of the OB, normalized to intensity in the ONL. Error bars represent SEM. ***C,*** Single optical section of a z-stack, with lateral projections showing Cx43 immunoreactivity in a tissue slice with a LY-filled OEC. Inset: higher magnification of the dashed rectangle indicated at the right. Arrowhead: a Cx43 cluster colocalizes with an OEC fine projection. ***D,*** Isosurface rendering of the green and red channels of a z-stack similar to the one in ***C***. The red surface was edited to eliminate the clusters not apposed to the cell. Arrowhead: contour surface of the nucleus generated with the blue channel. ***E,*** Electron micrograph of the ONL. Glial processes were contoured (blue); red lines: gap junction specializations. Inset: high magnification of the gap junction enclosed in the rectangle.

Table 1

Coefficients of linearity of I/V curves (see Materials and methods) and average passive properties of OECs.

	R^2	Ri (MΩ)	Vr (mV)	C (pF)
Non-linear (n = 19)	0.843 ± 0.014	102 ± 11	-81 ± 3	36 ± 2
Linear (n = 38)	0.970 ± 0.004 **	32 ± 3 **	-77 ± 2	39 ± 2
Control for MFA(linear OECs) (n = 8)	0.982 ± 0.022	24 ± 3	-80 ± 4	34 ± 4
MFA on linear OECs (n = 8)	0.921 ± 0.041 *	69 ± 9 **	-89 ± 10	29 ± 2

** $p < 0.001$ (Mann Whitney);

* $p < 0.01$ (Mann Whitney).